FISEVIER

Contents lists available at ScienceDirect

Chemistry and Physics of Lipids

journal homepage: www.elsevier.com/locate/chemphyslip



Microfluidic device as a facile *in vitro* tool to generate and investigate lipid gradients



Brittany M. Neumann^a, Devin Kenney^b, Qi Wen^c, Arne Gericke^{a,*}

- ^a Worcester Polytechnic Institute, Department of Chemistry and Biochemistry, USA
- ^b Bridgewater State University, Department of Chemical Sciences, USA
- ^c Worcester Polytechnic Institute, Department of Physics, USA

ARTICLE INFO

Keywords: lipid gradient Phosphoinositide PI(4,5)P2 Phosphatidylinositol-4,5-bisphosphate Phosphatidylserine Domains

ABSTRACT

This work describes a method that utilizes a microfluidic gradient generator to develop lateral lipid gradients in supported lipid bilayers (SLB). The new methodology provides freedom of choice with respect to the lipid composition of the SLB. In addition, the device has the ability to create a protein or bivalent cation gradient in the aqueous phase above the lipid bilayer which can elicit a gradient specific response in the SLB. To highlight these features we demonstrate that we can create a phosphoinositide gradient on various length scales, ranging from 2 mm to 50 µm. We further show that a Ca²⁺ gradient in the aqueous phase above the SLB causes anionic lipid clustering mirroring the cation gradient. We demonstrate this effect for mixed phosphatidylcholine/phosphatidylserine bilayers. The biomimetic platform can be combined with a Total Internal Reflection Fluorescence (TIRF) microscopy setup, which allows for the convenient observation of the time evolution of the gradient and the interaction of ligands with the lipid bilayer. The method provides unprecedented access to study the dynamics and mechanics of protein-lipid interactions on membranes with micron level gradients, mimicking plasma membrane gradients observed in organisms such as *Dictyostelium discodeum* and neutrophils.

1. Introduction

Many eukaryotic cells display distinct plasma membrane morphologies that depend on their life cycle. These morphologies are often dynamic, showing a high level of complexity and in some instances give rise to polarized cells. We are interested in understanding how cells control micron scale polarization of membrane organization as seen during processes such as cytokinesis and chemotaxis or within statically polarized epithelial cells. Phosphoinositides (phosphorylated diacylphosphatidylinositols, PIPs) and their interactions with proteins are pivotal for many of these dynamic and static membrane polarizations (Echard, 2008; Gassama-Diagne and Payrastre, 2009).

Phosphatidylinositol (PI) is the precursor of phosphoinositides, and it comprises $\sim 8\%$ of the plasma membrane (PM) phospholipids. To synthesize and interconvert phosphoinositides, a series of kinases and phosphatases specifically affect the phosphorylation status of the hydroxyl groups at the inositol ring positions 3, 4, or 5 (Dyson et al., 2012; Sasaki et al., 2009). Phosphatidylinositol-4,5-bisphosphate (PI(4,5)P₂) represents $\sim 2\%$ of the PM phospholipids and has a relatively stable global concentration. Phosphatidylinositol-4-phosphate (PI(4)P), the

primary precursor for $PI(4,5)P_2$, shows the second highest PM concentration among the phosphoinositides, while the other five phosphoinositide species are exceedingly rare, as they represent less than 1% of the PM lipids. Nevertheless, one of these very rare species, phosphatidylinositol-3,4,5-trisphosphate ($PI(3,4,5)P_3$), is a potent second messenger for cell motility, proliferation, and growth. The consequence of an altered metabolism where there is an overproduction of $PI(3,4,5)P_3$, and thus a constitutively activated PI3K-Akt signaling pathway, leads to pathologies such as cancer and overgrowth syndromes (Saarikangas et al., 2010; Viaud et al., 2016).

A laterally non-uniform distribution of phosphoinositides is the hallmark of many important cellular events. In cytokinesis, for example, $PI(4,5)P_2$ production and polarization are crucial for spindle orientation, mitotic cell shape and bridge stability after furrow ingression. Subsequently, $PI(4,5)P_2$ hydrolysis is essential for normal cytokinesis abscission (Cauvin and Echard, 2015; Saarikangas et al., 2010; Tsujita and Itoh, 2015; Viaud et al., 2016). Chemotaxing cells, such as *Dictyostelium discoideum* or neutrophils, show distinct and dynamic phosphoinositide polarization characterized by the accumulation of PI 3-kinase and phosphatidylinositol-3,4,5-trisphosphate ($PI(3,4,5)P_3$) at the

^{*} Corresponding author at: Worcester Polytechnic Institute, 100 Institute Rd 01609, Worcester, MA, USA. *E-mail address:* agericke@wpi.edu (A. Gericke).

leading edge of the migrating cell (Cauvin and Echard, 2015; Devreotes and Horwitz, 2015; Saarikangas et al., 2010; Tsujita and Itoh, 2015; Viaud et al., 2016). An example for polarized cells with a globally static polarized structure are absorptive epithelial cells. Epithelial cells increase their surface area by developing the so-called "brush border" membrane, which is a highly structured plasma membrane characterized by long, thin, highly curved structures (typically 100 nm in diameter and 100 nm–2000 nm in length). The apical side of epithelial cells shows increased PI(4,5)P₂ concentrations, while the basolateral side exhibits increased PI(3,4,5)P₃ concentrations in the PM (Krahn and Wodarz, 2012; Saarikangas et al., 2010; Tsujita and Itoh, 2015; Viaud et al., 2016).

Phosphoinositides have been shown to bind a broad range of protein targets that are involved in an extraordinary array of physiological functions (De Craene et al., 2017) including those crucial to cell motility. Temporal and spatial control of phosphoinositide levels consequently regulates the phosphoinositide-binding protein functionalities. This spatiotemporal organization is an important aspect for the proper execution of these signaling events. While several studies have described polarized phosphoinositide distribution in living cells in response to external stimuli, many aspects of the generation and maintenance of such gradients, in particular with respect to the physical chemistry of the underlying processes, have not been sufficiently detailed. Despite the obvious benefits of combining the results from in vivo and in vitro studies, there is, to the best of our knowledge, currently no in vitro platform available that provides the experimental freedom required to investigate the many biophysical facets of lateral membrane gradients. To understand the biophysical underpinnings of membrane gradients with respect to mediating signaling events, it is important to have complete experimental freedom with respect to composition and physical properties of the lipid bilayer as well as the nature of the chemical species (e.g., proteins, bivalent cations) interacting with that bilayer. It is the goal of this project, to develop a device that allows for the systematic investigation of how gradients can be created, how they are maintained and how proteins affect and interact with such lipid gradients (Saarikangas et al., 2010; Tsujita and Itoh, 2015; Viaud et al.,

Solid supported lipid bilayers have been established as facile tools for the biophysical characterization of model membrane systems (Castellana and Cremer, 2006; De Craene et al., 2017; Hardy et al., 2013; Kalb et al., 1992; Shekhar et al., 2011). The Sanii (Liu et al., 2015) and Huskens (Krabbenborg et al., 2014) groups both utilized SLBs to develop biomimetic devices for the preparation of lipid membrane gradients. With the device developed by the Sanii (Liu et al., 2015) group, a membrane gradient can be created that enables the investigation of gradient diffusion, protein-lipid interactions, and gradient dependent domain formation. Their method uses a three-dimensional PDMS stamp to deposit two spatially separated multilamellar lipid stacks onto a glass cover slip. Upon rehydration, the stacks "heal" the divide between them forming a contiguous unilamellar SLB with a gradient between the two deposited multilamellar lipid stacks (Liu et al., 2015).

The Huskens (Krabbenborg et al., 2014) group developed an experimental platform that can 'lock-in" the desired lipid gradient profile in an array of micron-sized Cr corrals. In their work, they use a mixture of zwitterionic and negatively charged lipids with a high melting point to obtain the lipid bilayer. Heating the system to above the phase transition temperature causes the lipids to enter a mobile fluid phase, and a gradient of the negatively charged lipids within the lipid bilayer is obtained by applying a voltage that draws the charged lipids to one side of the corral. Upon cooling below the phase transition temperature of the lipid mixture, the lipids enter the gel phase, "locking-in" the gradient (Krabbenborg et al., 2014).

The Sanii group's experimental platform is simple and has generally no limitations with respect to the composition and physical properties of the lipid stacks (e.g., lipid phase transition temperature and charge).

However, the shape and slope of the lipid gradient cannot be controlled by this device. The method introduced by the Huskens group allows for a highly tunable lipid gradient; the length scale of the membrane gradient is in a physiologically relevant range, and the gradient can be "locked-in", which is potentially a major advantage for sensor applications. However, the method requires lipids with high gel/liquid-crystalline phase transition temperatures and the use of an electric field to create a lipid gradient of anionic lipids. In both methods, the gradient formation is restricted to the SBL, *i.e.*, the fluid phase above the lipid bilayer cannot exhibit a gradient of one or more of its constituents (*e.g.*, a non-uniform distribution of a lipid modifying enzyme).

The device that we have developed combines the advantages of both existing techniques. These include the freedom of choice with respect to the lipid composition and physiologically relevant length scales over which the gradient is generated. In addition to this, our device adds the ability to create a protein or bivalent cation gradient in the aqueous phase above the lipid bilayer. It is even possible to fabricate a gradient in the lipid bilayer with an opposing gradient in the aqueous phase. The steepness of the gradient, within the limits of its physical design, can be adjusted based upon the experimental objectives. To show the broad applicability of this microfluidic device, we will demonstrate that we can create phosphoinositide gradients on various length scales, ranging from 2 mm to 50 μ m. We further show how a gradient in the aqueous layer above a homogeneous lipid bilayer can impart a non-uniform response in the lipid bilayer. This biomimetic platform can be combined with Total Internal Reflection Fluorescence (TIRF) microscopy, which allows for the convenient observation of the time evolution of the gradient and the interaction of ligands with the lipid bilayer.

2. Materials and methods

2.1. Lipids

1.2-dioleovl-sn-glycero-3-phosphocholine, purity > 99% (DOPC), 1palmitoyl-2-oleoyl-sn-glycerol-3-phosphocholine, purity > 99% (POPC), 1,2-dioleoyl-sn-glycero-3-phosphoethanolamine-N-(lissamine rhodamine B sulfonyl) (ammonium salt) (Excitation 560 nm, Emission 583 nm), purity > 99% (Rh-PE), 1-palmitoyl-2-oleoyl-sn-glycero-3-phospho-Lserine (sodium salt), purity > 99% (POPS), 1-palmitoyl-2-(dipyrrometheneboron difluoride) undecanoyl-sn-glycero-3-phospho-L-serine (ammonium salt), purity > 99% (TopFluorPS) (Excitation 495 nm, Emission 503 nm), L-α-phosphatidylinositol-4,5-bisphosphate (Brain, Porcine) (ammonium salt), purity > 99% (PI(4,5)P₂), 1-oleoyl-2-(6-[4-(dipyrrometheneboron difluoride)butanoyl]amino)hexanoyl-sn-glycero-3-phosphoinositol-4,5-bisphosphate (ammonium salt), purity > 99% (TopFlour PI(4,5)P₂, Excitation 544 nm, Emission 571 nm), cholesterol, purity > 98% (ovine wool), were purchased from Avanti Polar Lipids (Alabaster, AL) and used as received. The quality of the lipids was checked by TLC. The solvent mixtures used for POPC, DOPC and POPS TLC runs were 2:1 chloroform:methanol and 1:1 chloroform:methanol. When there is degradation of lipids, we have found streaking and a loss of separation on the TLC plates. PI(4,5)P2 is tested using 65:25:4 chloroform:methanol:amonium hydroxide and 1:1 chloroform:methanol solvent mixtures. When PI(4,5)P2 is of high quality, it will migrate to slightly above the starting line in the first mixture and fails to migrate in the second. When PI(4,5)P2 degrades, the sample will fail to migrate using the first more polar mixture and appears as a streak in the second solvent mixture. For additional information on TLC and solvent mixtures visit the Avanti website for full technical detail (Ellingson and William, 1968; Mangold, 1961; Mangold and Malins, 1960; Sims and Larose, 1962; Skipski et al., 1962). In addition to the quality check using TLC, the concentrations of the respective lipids in the stock solutions were determined by a phosphate assay as described by Avanti Polar Lipids (Subbarow, 1925; Sbalzarini and Koumoutsakos, 2005). With the exception of PI(4,5)P2, the lipids were dissolved in chloroform and these stock solutions were checked with TLC once every two weeks (chloroform stock solutions were kept no longer than a month, except for the fluorescently labeled lipids due to their expense). $PI(4,5)P_2$ was dissolved in 20:9:1 (chloroform: methanol: water).

2.2. Salts

High purity water was obtained from an in-house system, PICOPURE*3 Hydro*Service. The salts used to make the buffers were EDTA disodium salt dihydrate, purity 99% (VWR, Randor, PA), citric acid, purity 99% (Sigma, St. Louis, MO), calcium chloride dihydrate, purity 99% (FisherBiotech, Waltham, MA), HEPES, purity 99% (AlfaAesar, Ward Hill, MA), sodium chloride, purity 99% (Amresco, Fountain Park, Solon, OH), and sodium azide, purity 99% (Thermo Fisher Scientific, Waltham, MA). We utilized three types of buffer solutions for our studies: Loading buffer (20 mM citrate (pH 4.0), 500 mM NaCl, 1 mM azide), physiological buffer (20 mM HEPES (pH 7.4), 150 mM NaCl, 0.1 mM EDTA), physiological buffer with 5 μ g/ml of bovine serum albumin (BSA), and physiological buffer with either 1 mM Ca²+, 2 mM Ca²+, or 3 mM Ca²+. The BSA was made from a dilution of (BioRad, Hercules, CA) 2 mg/ml stock solution.

3. Experimental

3.1. Microfluidic device fabrication

The Sylgard 184 silicon elastomer kit (Dow Corning, Midland, MI) was used to make the polydimethylsiloxane (PDMS) component of the microfluidic device. The channels are imprinted from a silicon master during the molding process. To do this, curing agent (10% by weight) was added to the elastomer base and then mixed vigorously. This was followed by degassing for an hour. The uncured PDMS was poured onto the silicon master, degassed for an additional 10 min and then cured in the oven at 72 °C for 45 min. The now hardened PDMS was cut from the silicon master, and the inlet and exit holes were punched with a blunt 19 gauge BD PrecisionGlide needle. This PDMS mold, with the silicon master design imprinted on its surface, was further cleaned with Scotch tape to remove dust and debris. This is the top of the microfluidic device.

The base of the microfluidic device is a $24 \times 40 \text{ mm}$ N0.1.5 Gold Seal cover glass slide used for TIRF microscopy. The TIRF slide was piranha cleaned for an hour, rinsed with copious amounts of HPLC water and stored in HPLC water. The slide is then rinsed with methanol and dried under N_2 gas.

At this point, the PDMS mold and TIRF slide are plasma cleaned with an air plasma. First, the TIRF slide is placed in the chamber and plasma cleaned for two minutes. Then the Scotch tape is removed from the PDMS, and the PDMS is added to the chamber. The PDMS and TIRF slide are cleaned for an additional 45 s. The two pieces are then gently pressed together forming an irreversible attachment.

3.2. Vesicle preparation

To make vesicles, the appropriate amounts of lipid stock solutions are dispensed into an amber vial. To remove the solvent, the sample is heated ($\sim\!30~\text{C}$) while under a gentle stream of $N_2.$ The vial with the lipid film is then placed overnight in a vacuum oven at $\sim\!50~\text{C}$ to remove any residual solvent. The lipid film is resuspended in loading buffer and vortexed for 60 s. This is repeated three times with four minutes of rest in between. The multilamellar vesicles are then extruded (Avanti Extrusion Kit) through a 50 nm polycarbonate membrane (Avanti, Alabaster, Al) for a total of 31 passes. The size distribution of the resulting unilamellar lipid vesicles is checked by dynamic light scattering (DLS). Using this method, unilamellar vesicles with a narrow size distribution and an average hydrodynamic diameter of $\sim\!80\,+/-15$ nm are obtained. These vesicle suspensions are kept no longer than 24 h.

3.3. Solid supported lipid bilayer (SLB) fabrication

To form SLBs, loading buffer is passed through the microfluidic device through the outlet. By passing this solution in the reverse direction of the setup, we ensure that all air bubbles are pushed out of the device. In addition, this priming allows us to check for leaks since the pressure from pushing the fluid by hand into the device is much higher than that achieved by the syringe pump during the experiment. To introduce any liquid from the inlet side into the microfluidic device, a 1 ml syringe with a 25-gauge needle is attached to the inlet using PTFE#3 AWG thin wall tubing from Cole-Parmer. This tubing OD and the needle OD were matched to ensure a liquid-tight seal. In our observation, leaking only occurs when there is back pressure due to a clog. The vesicle suspension can be introduced through the inlets. Here three syringes are attached to two feet of tubing. When making homogeneous SLBs, the three syringes are filled with vesicle suspensions of equal concentrations (1 mM). When the syringe pump is run at 10 µl/min and with two feet of tubing, it takes twenty minutes for the vesicles to reach the observation chamber. This "dead-time" can be adjusted by either changing the length of the tubing or speed of the syringe pump. This method was used in our initial test experiments to follow SLB formation by fluorescence microscopy. A more convenient method is to introduce the vesicle suspension through the outlet of the microfluidic device by a hand driven syringe. This is the procedure we used to obtain laterally homogeneous lipid bilayers once we had confidence in the SLB formation.

The exact mechanism of SLB formation is discussed in detail in several articles (Drucker et al., 2014; Jönsson et al., 2009; Kalb et al., 1992; Keller et al., 2000; Richter et al., 2006). In brief, small unilamellar vesicles interact with the solid support. The vesicles will fuse and break open at a critical surface concentration which is dependent on the lipid composition and the type of solid support. Typically, the barriers for high quality supported lipid bilayers on glass is related to the negative potential of the vesicle. If the negative potential is high, it is difficult to get the vesicle to interact with a glass surface. The result is unbroken vesicles and a defective supported lipid bilayer. This can be seen qualitatively by patchiness of the bilayer as well as a lack of fluidity. To overcome this, the pH and salt concentration of the bulk solution can be optimized to encourage high vesicle coverage and successful bilayer development. For vesicles with a high anionic lipid concentration, buffer solutions with low pH (pH ~ 4.5) and high salt concentration (~500 mM) should be used. Once high vesicle coverage is achieved on the surface and deformation and fusion of the vesicles has begun, HPLC water is flushed over the system as final push to develop the bilayer (Knight and Falke, 2009; Knight et al., 2010; Ziemba and Falke, 2013). In addition to this, there is an added advantage of using a microfluidic device. It has been found that SLBs have a better quality when developed in these devices. For example, SLBs with lipid compositions that contain cholesterol and/or highly charged lipids are sometimes difficult to obtain without macroscopic defects, while we did not encounter any problems when the microfluidic device was used. The hypothesis is that the shear forces from the directed flow pushes the developing bilayer front into intact SUVs. The collision causes them to break open and aid in the development of the supported lipid bilayer with fewer defects (Jönsson et al., 2009).

After 100 μl of the vesicle suspension has passed, it is allowed to sit for 30 min in the observation chamber. Then 100 μl of HPLC water is passed to break any remaining intact vesicles with osmotic stress. This is followed by 100 μl of the physiological buffer. While we were not able to discern any macroscopically visible imperfections in the lipid bilayer (e.g., holes), it cannot be ruled out that such imperfections exist below the resolution limit of the microscope. To fill in these potential holes, 100 μl of a BSA solution (5 $\mu g/m l)$ was introduced into the observation chamber and allowed to sit for 30 min. This is followed by a final wash with 100 μl of our physiological buffer (\sim 20 times the cell volume). To maintain the integrity of the SLB, it is important that no air

bubbles move through the device as these various solutions are introduced (Castellana and Cremer, 2006).

3.4. Generation of a lipid gradient using a $PI(4,5)P_2$ analog

The critical micelle concentration (CMC) for TopFluorPI(4,5)P2 is not known, however, using dynamic light scattering we found that nanomolar concentrations of TopFluorPI(4,5)P₂ dissolve as a monomer. We take advantage of this property, by creating three TopFluorPI(4,5) P2 solutions of different concentrations below the CMC, which are then used to generate a gradient of fluorescently labeled PI(4.5)P₂ embedded in an otherwise homogeneous lipid bilayer, Aqueous TopFluorPI(4.5)P₂ solutions with three different concentrations are obtained by drying appropriate amounts of the lipid from organic stock solutions as described above and re-dissolving the lipid film in the loading buffer. The aqueous samples are then drawn up into three 1 ml syringes, and any air bubbles present in the syringe are removed. Then a 25G needle with two feet of tubing is attached to the syringe. The syringe plunger is depressed so that the solution is pushed through to the end of the tubing. All three syringes are placed in the syringe pump, and the bar is placed against the plungers so that there is a small drop at the end of each tube. The tubes are inserted into the microfluidic inlets, and the syringe pump is started. The syringe pump is run for 20 min at 10 $\mu l/$ min. During this time the TopFluorPI(4,5)P2 partitions into the homogeneous SLB that has been previously made. To push any labeled lipid that did not insert into the lipid bilayer out of the observation chamber, the syringe pump is stopped, and the syringes with the lipid solutions are replaced with three new syringes that are loaded with physiological buffer solutions. The physiological buffer solution is run for 20 min at the same rate as the lipid solution before. After this point, the syringe pump is stopped, and the fluorescence imaging of the bilayer starts. For these experiments, a 60× TIRF objective is rastered across the observation chamber perpendicular to fluid flow.

While the method described above is suitable for the microfluidic device with the large observation chamber because of the long equilibrium times for the gradient, a different method is needed for the microfluidic device with the sub-millimeter chambers (for the narrower chambers the equilibration occurs on a time scale of minutes rather than hours). In order to deposit the labeled PI(4,5)P2 and flush the SLB with buffer, the transition between these solutions needs to be immediate. To achieve this the labeled solution with the labeled PI(4,5)P₂ is first pushed through the syringe to the end of the tubing before attaching it to the microfluidic system. The syringe is then switched with a buffer loaded syringe. This is then attached to the inlets of the platform. The result is that when the syringe pump is started labeled PI(4,5) P2 is introduced and immediately chased with buffer in a process we deem as a load (deposition of labeled PIP2) followed by flush (wash with buffer). The imaging is started when the syringe pump is started. With the load-flush experiment, the buffer is run for twenty minutes and then stopped with an image taken once every minute for an hour at the start of the syringe pump.

The final method used to create lipid gradients is direct vesicle deposition. In this case three different vesicles compositions are made at the same concentrations (i.e. 10%PI(4,5)P₂, 0.1%TopflourPI(4,5)P₂, 89.9%POPC; 3%PI(4,5)P₂, 0.03%TopflourPI(4,5)P₂, 97%POPC; and 100%POPC at 1 mM concentration). This method allows for control over the composition of the SLB where the initial composition can be plotted and correlated to fluorescence intensity. The change of fluorescence intensity over time can then be followed and thus have a correlation of the phosphoinositide distribution in the bilayer. The three different vesicle compositions are made as described earlier. They are introduced to a buffer primed microfluidic device the same way a homogenous bilayer is introduced *via* the three inlets. The same washing and prepping steps are followed as in the other preparative SLB techniques.

3.5. Generation of Ca²⁺ gradients

The SLB films were prepared as described before. Three membranes were tested for the interaction with a Ca $^{2+}$ gradient: 5% PI (4,5)P $_2$ / 94.9% DOPC/ 0.1%TopFlour $^{\circ}$ PI(4,5)P $_2$; 5% PI(4,5)P $_2$ / 30%Cholesterol/ 64.9%DOPC, 0.1%TopFlour $^{\circ}$ PI(4,5)P $_2$ / 30%POPS/ 69.9%POPC/ 0.1%TopFlour $^{\circ}$ PS. Physiological buffer solutions (see above) with 1 mM, 2 mM, and 3 mM calcium concentrations were prepared and loaded into the three syringes connected to the inlets of the microfluidic device. The Ca $^{2+}$ buffer solutions were pumped through the microfluidic device with 10 μ l/min rate while simultaneously obtaining TIRF images of the respective lipid bilayer. Images were taken every 5 min for an hour for the PI(4,5)P $_2$ SLBs. For the PScontaining membranes, the objective was rastered in a 2.0 mm \times 2.5 mm rectangle once every 20 min for 22 h. The images at each time point were stiched together and analyzed.

3.6. TIRF microscopy

The fluorescence images were obtained using a Nikon (Minato, Tokyo, Japan) Eclipse Ti inverted microscope with a TIRF Illuminator. For excitation sources, coherent 488 nm and 561 nm sapphire lasers were used. Images were captured with an Andor 3iXon CCD camera (Belfast,UK). A Nikon $4\times$ CFI Plan Fluor objective with a numerical aperture of 0.13 was used for epi-fluorescence images and a Nikon $60\times$ CFI Apo TIRF oil objective with a 1.49 numerical aperture was used for TIRF imaging. Both the 488 nm filter cube and 561 nm filter cube were purchased from Chroma (Foothill Ranch, Ca).

3.7. Data analysis

The stitching of the rastered images to a single image was done using the Nikon Elements software. All other image processing was done in ImageJ (NIH Bethesda, MD). For the topology images, a movie at nine positions across the channel was acquired. The mean fluorescence intensity was calculated for each frame of the movie. These data were imported into Origin software (Northhampton, MA) and a topology graph of the mean fluorescence intensity was plotted against time and position.

For the ${\rm Ca}^{2+}$ experiments, the data was acquired by the same means as above. Instead of calculating the mean fluorescence intensity, an intensity threshold was set to the top 1.3% of intensity brightness. This was then converted into a binary image where the brightest areas are counted as domains by selecting the areas that exceeded the intensity threshold value, had a pixel diameter greater than 5^2 pixels and a circularity between 0.5 and 1. These domains were counted, the average diameter calculated, and percent area of the frame determined for each frame of each movie. These data were imported into the Origin software, and two topology graphs were constructed: number of domains as a function of time and position, and the percent area of the frame as a function of time and position (Schindelin et al., 2015).

4. Results and discussion

4.1. Microfluidic setup

The work of Byfield et al. (2009) was the inspiration behind using a microfluidic gradient generator to make laterally heterogeneous supported lipid bilayers (SLB). The "Christmas tree" design of this microfluidic platform, originally fashioned by Dertinger et al. (Dertinger et al., 2001; Jeon et al., 2000) takes three different initial concentrations and forms a gradient in the observation chamber of the device. The lamellar flow of the fluid prevents mixing perpendicular to the flow direction once the fluid enters the observation chamber (Fig. 1). At the first level of the mixing tree, there are three inlets that split and recombine the initial sample concentrations to form four new

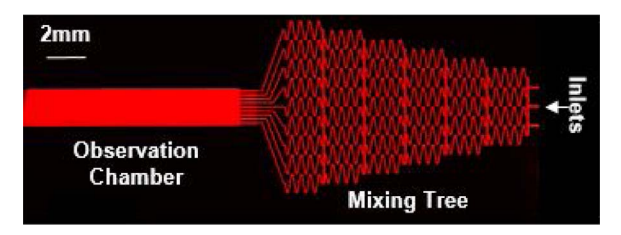


Fig. 1. Wide-field fluorescence image of the microfluidic gradient generator with a homogenous SLB composed of DOPC and 1%RhodaminePE. The three initial concentrations are introduced into the inlets. They are of equal concentrations and composition, resulting in no gradient. The high fluorophore percentage was used for aesthetic reasons to highlight the features of the microfluidic platform design.

concentrations. This process is repeated at each subsequent level, ending in a total of nine outlets which recombine into the large observation chamber. When a concentration series is introduced into the microfluidic device, (see Fig. 2 for the physical setup of the device and Fig. 3 for images of a lipid sample gradient) the concentration gradient brackets the lowest and highest concentrations of the three samples introduced through the device inlets. The steepness of this gradient is highly tunable by controlling the flow rate of the fluid through the device, where at the highest speeds the gradient forms a step function (Jeon et al., 2000). The lamellar flow of the fluids as they exit the nine channels to enter the observation chamber is essential for successful gradient development. The lack of turbulent mixing perpendicular to the fluid's flow direction means that the only physical pathway for the gradient to equilibrate is by the Brownian motion of the dissolved molecules or suspended vesicles. The lamellar flow of the fluid is a key physical characteristic of the device since it provides maximum flexibility with respect to the kind of gradient that is being generated, being it dissolved molecules or suspended unilamellar vesicles (Sackmann et al., 2014; Toh et al., 2014) (Fig. 3).

4.2. Generation of a PI(4,5)P2 gradient in a DOPC SLB

To generate a PI(4,5)P $_2$ gradient, first, a homogenous SLB composed of DOPC and Rhodamine-PE (Rh-PE/10ppb) was created in the microfluidic device (Fig. 3B). The Rh-PE is added to the SLB lipids to check for macroscopic defects and to check the bilayer's fluidity using smTIRFM (in our experiments we bleach a portion of the SLB and check for recovery in that area after 10 min). To visualize the gradient of phosphoinositides, we utilized fluorescently labeled TopFluor-PI(4,5)P $_2$ (10 nM, 30 nM, 60 nM). We have found that the lipid is monomeric in aqueous solution at these concentrations. Due to the negative charge of the TopFlourPI(4,5)P $_2$ headgroup and the steric hindrance imposed by the large fluorescent label on the acyl chain, the mutual interaction of these lipids is dominated by repulsive electrostatic forces, resulting in a critical micelle concentration (CMC) significantly higher than the nanomolar concentrations used in our experiment (please note that the cmc for unlabeled PI(4,5)P $_2$ is in the 30–40 μ M) (Moens and Bagatolli,

2007). A gradient of monomeric (dissolved) TopFlourPI(4,5)P $_2$ can, therefore, be obtained in the aqueous phase when these three different concentrations of the lipid are introduced into the three inlets of the microfluidic device (Fig. 3). The partition coefficient between the aqueous solution and the SLB of the lipid still leans toward membrane incorporation, so, as the TopFluor-PI(4,5)P $_2$ flows over the DOPC SLB, the labeled lipid will spontaneously insert. The lamellar flow of the microfluidic device ensures that there is no cross channel mixing (Fig. 3A), maintaining the aqueous PI(4,5)P $_2$ gradient during the insertion process (Fig. 3C).

Fig. 4 shows the results of TIRF imaging of the SLB after the insertion of the TopFluor PI(4,5)P₂. We acquired Image 4A by rastering the 60 × TIRF objective perpendicular to the fluid flow, taking an image at nine equally spaced positions. This scan was repeated once every 30 min for 24 h to monitor the time evolution of the PI(4,5)P₂ gradient. As can be seen qualitatively, the TopFluor PI(4,5)P2 gradient is maintained as the lipid inserts into the preformed SLB and slowly equilibrates over 24 h (see also a movie in Supplementary material). Fig. 4B shows the mean fluorescent intensity per image frame across the observation channel (i.e., perpendicular to the flow direction). The initial distribution of the fluorescently labeled lipid is close to the distribution expected from a sigmoidal model. Fig. 4C shows the temporal evolution of the TopFluorPI(4,5)P2 gradient as a topology graph (see also the corresponding movie in the Supplementary material). For this graph, a single raster across the channel perpendicular to the fluid flow was charted against time and color coded to indicate the fluorescence intensity. The color map shows the time-dependent equilibration of the gradient. It takes over 22 h for the gradient of TopFluorPI(4,5)P2 to equilibrate across the chamber. This is expected for a lipid diffusing via Brownian motion at about 2.7–2.8 μm²/s (Harishchandra et al., 2015; Schutz et al., 1997; Ziemba and Falke, 2013) in a chamber of 2 mm width. We found these measurements to be highly reproducible (n = 5). For each set of parameters, i.e., TopFluorPI(4,5) P_2 start concentration, flow speed, and SLB composition, the gradient is consistent and repeatable as measured by the equilibration time of the gradient.

The second option to obtain a PI(4,5)P $_2$ gradient is to use vesicles with different compositions at the three inlet ports of the microfluidic device. To illustrate this approach, three unilamellar vesicle suspensions with the following compositions were made: 10%PI(4,5)P $_2$, 0.1%TopFlour PI(4,5)P $_2$, 90%POPC; followed by 3%PI(4,5)P $_2$, 0.03%TopFlour PI(4,5)P $_2$, 97%POPC; and 100% POPC (all percentages are mol%). These three intial vesicle compositions, when combined in the mixing tree, will result in nine ratios of the three compositions spanning across the outllets of the device. This is in contrast to the lipid monomer insertion, where there is nine different concentrations of the monomeric lipid after mixing. In comparison to the monomeric lipid insertion method, where the degree of lipid insertion is unknown, this method has the advantage that the precise lipid composition in the SLB is known; in this case, the range of the gradient is 10%PI(4,5)P $_2$ -0%PI (4,5)P $_2$.

Fig. 5C shows quantitatively the temporal evolution of the lipid





TIRF microscope. (A) Demonstration of the connection between the syringe pump and the microfluidic platform. The fluids in the syringe set vary in concentration and or composition to develop a gradient. The syringes are connected *via* 2 ft of tubing to the microfluidic device, and the rate of flow is controlled by the syringe pump. (B) The tubing connections to the microfluidic platform as well as the outlet tubing which empties into a waste vial. The objective is centered over the observation chamber to record the changes of the SLB gradient. Since this setup is placed directly on the microscope, images can be acquired in real time at all stages of the experiment, which is critical for monitoring the gradient evolu-

Fig. 2. The setup of the microfluidic platform on the

tion under various conditions.

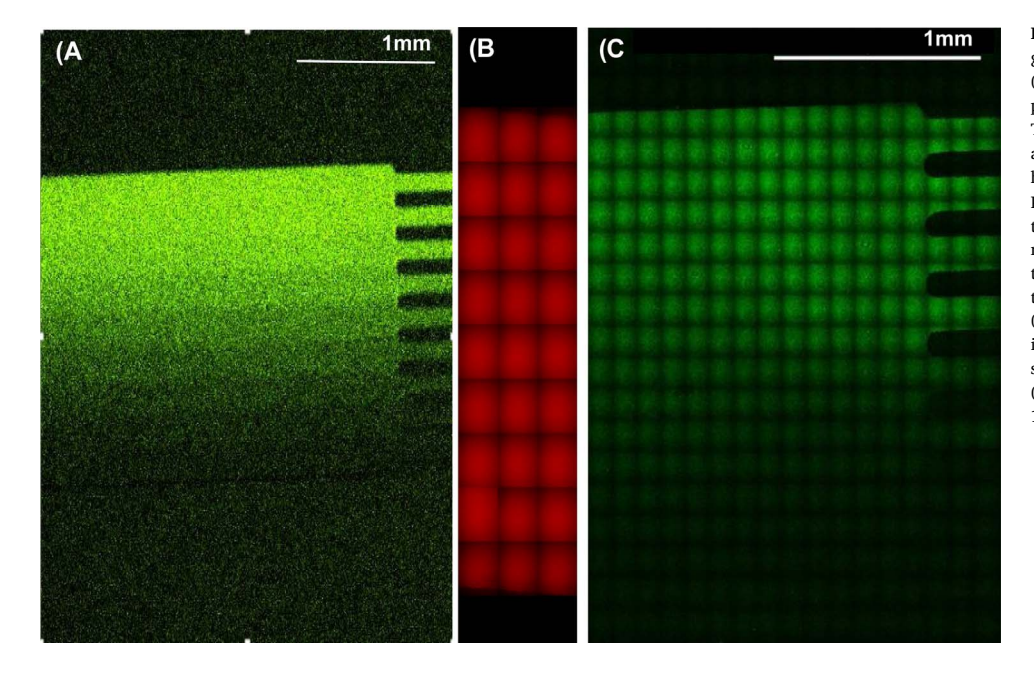


Fig. 3. TopFluorPI(4,5)P₂ gradient in a homogeneous DOPC bilayer labeled with Rhodamine PE. (A) Widefield fluorescence image of the microfluidic platform's observation chamber showing a TopfluorPI(4,5)P2 gradient in the aqueous phase above the SLB. (B) Stitched fluorescence image of the homogeneous DOPC bilayer labeled with 10 ppb Rh-PE. After the SLB was fully developed, the observation chamber was flushed with buffer solution to remove any remaining lipid vesicles. After the wash, the TopflourPI(4,5)P2 gradient with inlet concentrations of 10 nM, 30 nM, and 60 nM was introduced. (C) Stitched TIRF image of the DOPC bilayer with inserted TopFluorPI(4,5)P₂. The individual image squares are representative of one camera frame (single individual image before $138.24~\mu m~\times~138.24~\mu m$).

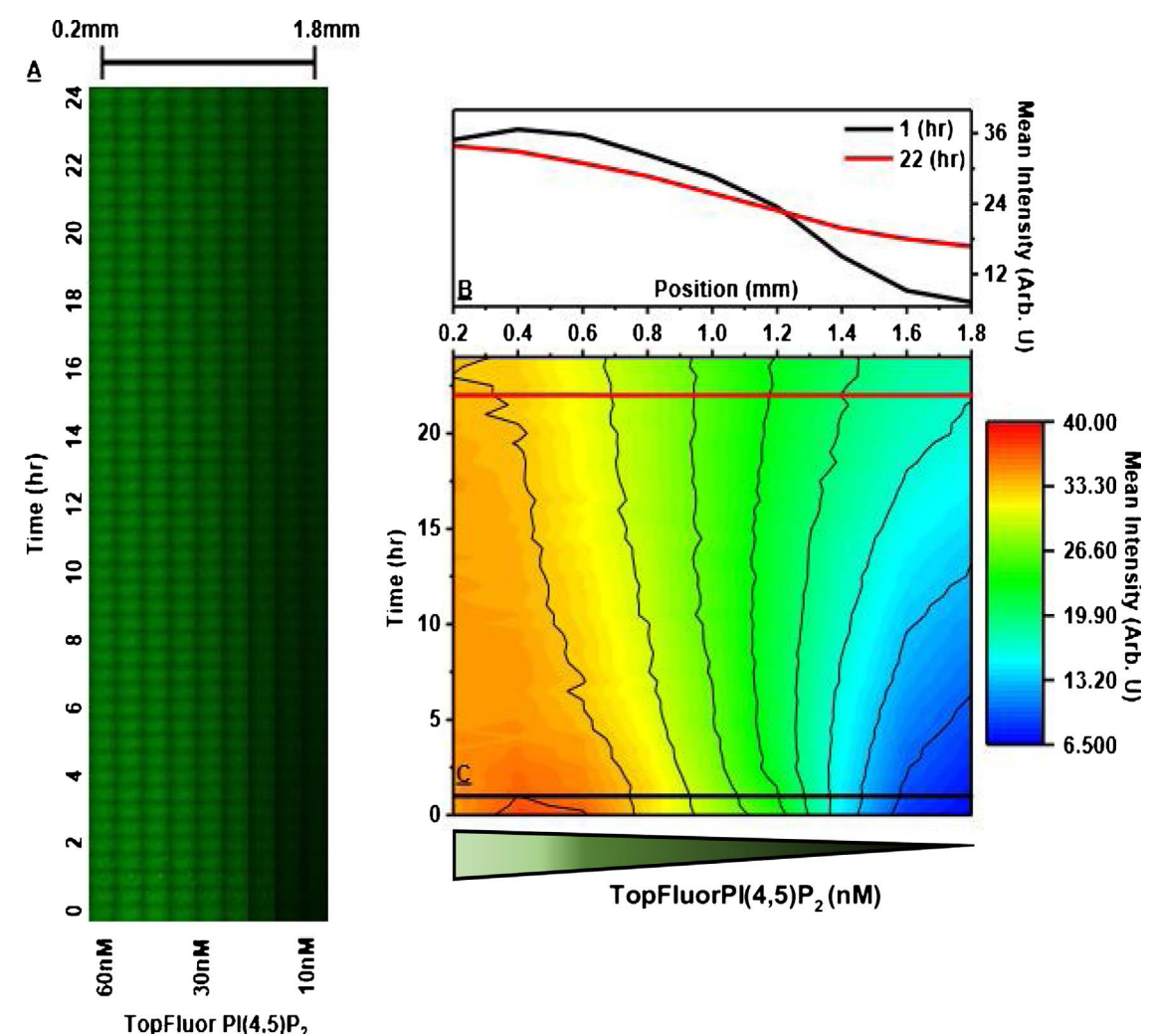


Fig. 4. Temporal evolution of the $PI(4,5)P_2$ gradient in the DOPC SLB. It takes over 22 h for the TopFlourPI(4,5) P_2 gradient to equilibrate across the 2 mm chamber. (A) Once an hour nine images were taken across the chamber and stitched together. Over time we see the brightest areas become dimmer and the darkest image parts become brighter indicating equilibration by diffusion (B) Integrated fluorescence intensities for each sub-image across the chamber at the beginning of the experiment. (C) Contour graph of the fluorescence intensity distribution as a function of time. The concentration ranges from 10 nM to 60 nM TopFlourPI(4,5) P_2 .

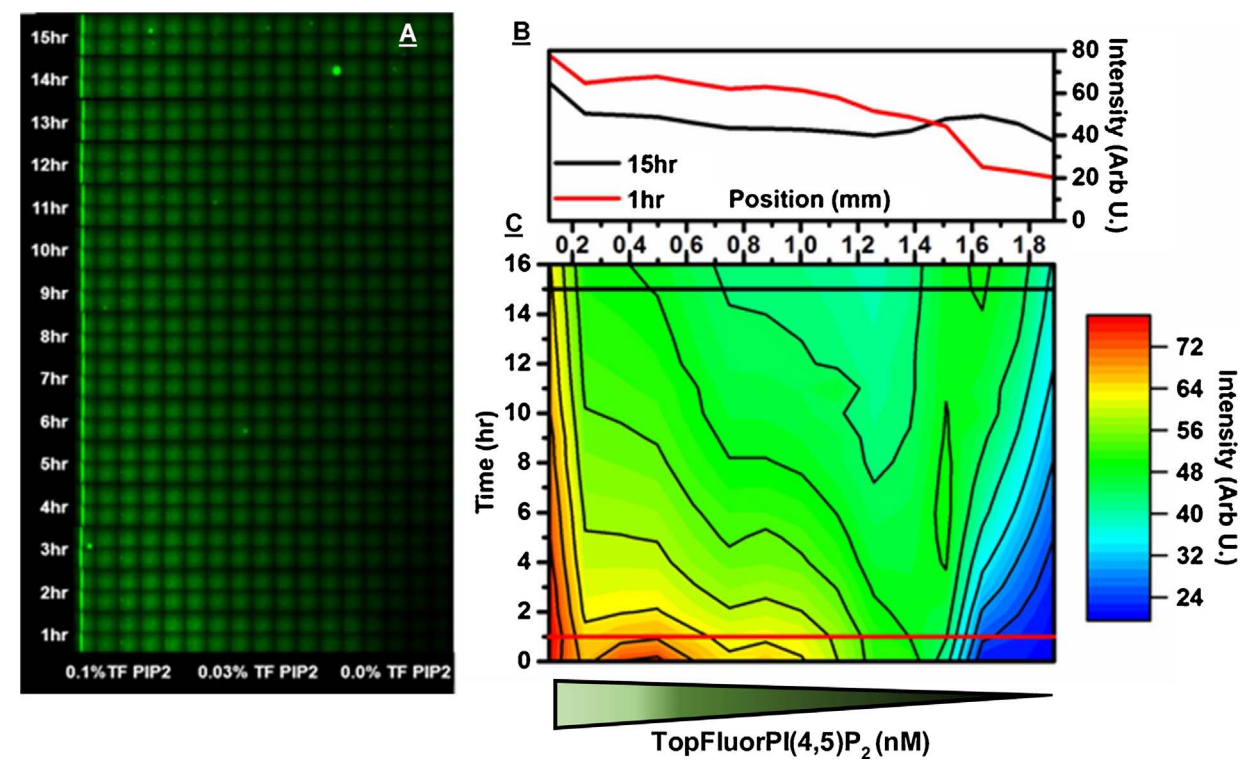


Fig. 5. Gradient of $PI(4,5)P_2$ obtained using vesicles with different $PI(4,5)P_2$ concentrations. Vesicle suspensions with equal vesicle concentrations but different vesicle compositions were introduced into the three inlets of the microfluidic device. The vesicle compositions were $10\%PI(4,5)P_2/0.1\%TopFlourPI(4,5)P_2/90\%DOPC$, $3\%PI(4,5)P_2/0.03\%TopFlourPI(4,5)P_2/97\%DOPC$, and 100%DOPC. The ratio of the unlabeled/labeled $PI(4,5)P_2$ is kept constant for all vesicle compositions. It is assumed that distribution of the unlabeled $PI(4,5)P_2$ mirrors the distribution of the labeled $PI(4,5)P_2$ analog. (A) Image obtained by taking once an hour 9 images across the chamber and stitching them together. (B) Integrated fluorescence intensities for each sub-image across the chamber at the beginning of the experiment. (C) Contour graph of the fluorescence intensity distribution as a function of time.

gradient, which is similar to the equilibration of the gradient obtained through lipid insertion (Fig. 4C). One might be concerned that the deposition of lipid vesicles with different compositions may lead to patchiness at the submicrometer scale. However, the image does not reveal any patchiness (though such patches would be at the limit of the resolution of the microscope) and there is no other indication of such heterogeneities. We believe that mixing of the lipids between adjacent vesicles occurs during the formation of the SLBs. In addition, if such small patches existed, local diffusion would lead to mixing at a sub minute time scale.

Both methods, the lipid insertion and deposition of vesicles with different compositions, exhibit advantages and disadvantages in terms of creating lipid gradients. The lipid insertion method creates very smooth gradients, while the deposition of vesicles with different lipid ratios leads to a less smooth gradient that has an initial appearance closer to a step function. In terms of the quality of the gradient, the lipid insertion method is therefore preferable. However, this method is limited by the type of the lipid that is being used and its concentration, since it requires the inserted lipid to be monomeric in solution. The major advantage of the vesicle deposition method is that one has complete freedom with respect to the type of lipid gradient that is being created. The experimental context will determine which method is the preferred one to answer a particular biophysical question.

4.3. Non-uniform calcium-dependent domain formation

To test whether a gradient of a solute interacting with a laterally homogeneous SLB can impart a gradient specific response in that SLB, we investigated the interaction of a Ca^{2+} gradient with SLBs composed of anionic lipids. The domain-forming effect of calcium upon interaction with anionic lipids like phosphatidylserine (PS) or PI(4,5)P₂ containing membranes is well established (Slochower et al., 2014). We hypothesized that the interaction of a Ca^{2+} gradient present in the bulk

phase above mixed PC/PS or PC/PI(4,5) P_2 SLBs leads to the formation of domains in a ${\rm Ca}^{2\,+}$ gradient-dependent manner.

The interaction of PS with Ca2+ is well studied, and it has been hypothesized that Ca²⁺ interacts with the PS headgroup *via* two modes. (1) Ca²⁺ is interacting with the carboxylic acid group of the serine. (2) Ca²⁺ can also interact with the phosphate linker of the glycerol backbone (Feigenson, 1986, 1989; Florine and Feigenson, 1987; Roux and Bloom, 1991; Sinn et al., 2006; Slochower et al., 2014; Vernier et al., 2009). While it is unclear which type of interaction is the dominant one, either interaction can lead to a bridging of adjacent PS molecules, causing a clustering of the lipid in mixed lipid bilayers. Visualization of PS clustering in an SLB with fluorescence microscopy is not trivial, and usually, high-resolution techniques like AFM are used to visualize these domains in fluid bilayers. To circumvent this problem, we used mixed POPS/POPC SLBs. POPS in the absence of Ca²⁺ has a gel/liquid-crystalline phase transition temperature of 14 °C (Marsh, 2013) i.e., POPC and POPS form a mixed fluid phase at room temperature. In Langmuir film experiments, the addition of Ca²⁺ leads to a condensation of PS monolayers (Hauser et al., 1969; Luna et al., 2011) and therefore, the addition of Ca²⁺ to a mixed POPC/POPS SLB is expected to give rise to domain formation in the leaflet distal to the glass support. We hypothesized that these PS domains would form in a Ca²⁺ gradient-dependent manner.

In Fig. 6, we show an SLB composed of 30% POPS, 0.1% Top-FlourPS, and 69.9%POPC as it interacts with a Ca^{2+} gradient. The Ca^{2+} concentrations of the solutions introduced into the inlet channels were 1 mM, 2 mM, and 3 mM, respectively, and the experiment was carried out at room temperature. In contrast to the previous experiment, where we stopped the flow of the buffer solution during imaging, the Ca^{2+} gradient flow was maintained throughout the entire duration of the experiment. This was to avoid that the Ca^{2+} in the fluid phase equilibrates across the observation channel. Fig. 6 is a montage of images that are obtained near the mixing channel outlets (see the corresponding

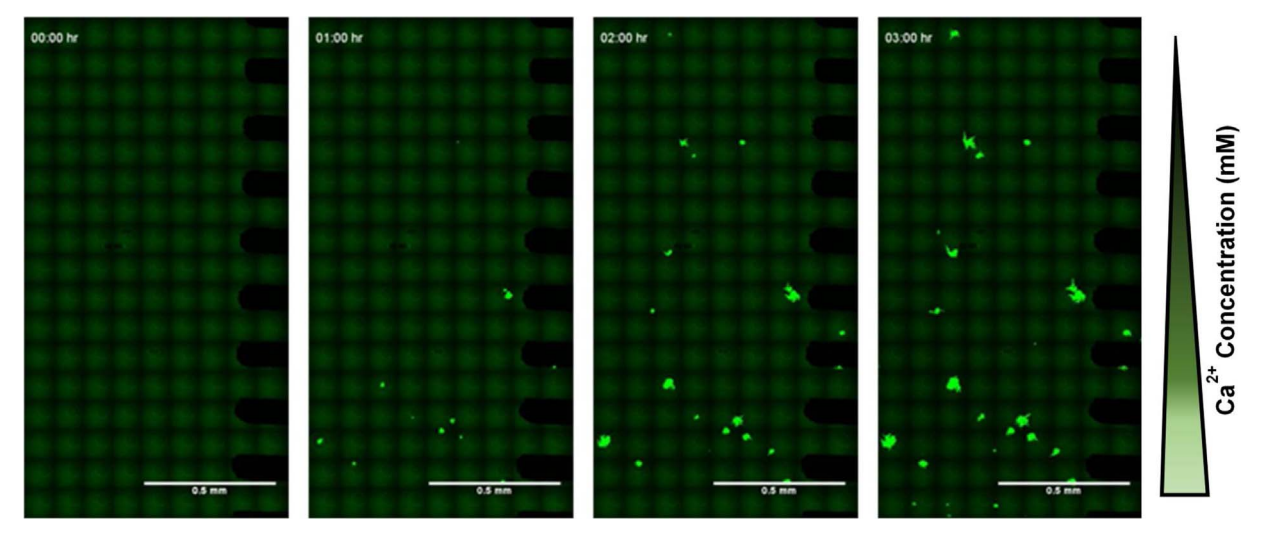


Fig. 6. Montage of stitched TIRF images showing heterogeneous domain formation due to a Ca^{2+} gradient flowing over a homogeneous SLB composed of 30%POPS/0.1%TopFlourPS/69.9%POPC. Each stitched image covers a range of 2.0×2.5 mm, and this raster was carried once an hour for 3 h (5 min total time to obtain a full stitched image). This experiment was repeated five times, where the domain formation is always biased towards the high Ca^{2+} concentration, yet it is difficult to determine exactly where the domains will appear within this high Ca^{2+} concentration range.

movie in the Supplementary material). The stitched image was obtained by combining individual images acquired across the channel using TIRF microscopy. This rastering was repeated once every 20 min over 3 h (it takes 5 min to obtain all images for the stitched image). POPS forms gel phase domains, as inferred from the jagged nature of the domain boundaries, upon interaction with the Ca2+ cations. The formation of these domains always starts in the area of the highest Ca2+ concentration, though the precise position within the high concentration region is difficult to predict. The mechanisms that lead to the seeding of these domains are unclear and exploring this aspect further is beyond the scope of this paper. After 30 min POPS/Ca²⁺ domains start to form and expand across the SLB as the Ca²⁺ continues to flow. The domains clearly form first in the regions with the higher Ca²⁺ concentration and a gradient of domains across the channel remains as the experiment progresses. To further explore this phenomenon where a heterogeneous aqueous ligand can impart asymmetry on a homogenous SLB, we expanded these Ca²⁺ experiments to include lipid compositions of PI(4,5) P₂ and PI(4,5)P₂/Cholesterol.

Fig. 7 is a montage of one image area over time for a 5% PI(4,5)P₂, 95% DOPC, 0.1% TopFlour PI(4,5)P₂ SLB. After 20 min of ${\rm Ca^{2}}^+$ exposure, we see the membrane punctuated with small areas of high fluorescence intensity. We believe that this is the result of TopFlour PI (4,5)P₂/PI(4,5)P₂ clustering due to the bridging effect of ${\rm Ca^{2}}^+$ (${\rm Ca^{2}}^+$ induced PI(4,5)P₂ clustering has been previously reported by the Janmey group (Braunger et al., 2013; Wang et al., 2014)). Like previous experiments, we obtained images by rastering the objective across the observation chamber and acquired an image at nine locations across the membrane perpendicular to the fluid flow. This process was repeated once every five minutes for an hour. Each position was compiled as a movie (see Supplementary material) and analyzed in ImageJ. Since the

domains for the PI(4,5)P₂/Ca²⁺ interaction are significantly smaller than that was found for the PS/Ca²⁺ interaction, we present the data in a slightly different way. We selected domains by setting a threshold for the intensity to create a binary image where the high-intensity regions were domains, and the low-intensity regions were interpreted as background. Fig. 8A shows the percent area covered by domains as a function of time and location within the chamber. Here we can see a dramatic increase in the percent area occupied by the PI(4,5)P₂/Top-FluorPI(4,5)P₂/Ca²⁺ domains. The domain area increases from 0 to 3% of the total image. The highest percent domain area correlates with the highest Ca²⁺ concentration. Domain formation in the regions with the lower Ca²⁺ concentrations occurs later than it is observed for, the higher Ca²⁺ concentration regions. Fig. 8B shows the number of domains counted at each position (heatmap) as a function of time (x-axis) and position (y-axis). This topology image shows that for all time points the largest number of domains are found in the regions with the highest Ca2+ concentrations. Domain formation starts at around 20 min and reaches a plateau at about 30 min. While domain formation in the areas with the lower Ca²⁺ concentration starts at the same time, the number of domains in these regions is significantly less than what is found for the areas with higher Ca²⁺ concentrations. The effects of the Ca²⁺ on PI(4,5)P₂ containing SLBs is evident by the spatiotemporal clustering of the PI(4,5)P₂ fluorophore in response to the Ca²⁺ gradient. In addition to this, we noticed edge effects in this experiment. The increased number of domains at the edge of the microfluidic device may be caused by the disruption of the speed of the lamellar flow at the wall of the PDMS. This could lead to a longer interaction between the Ca²⁺ and the $PI(4,5)P_2$ causing a more robust domain formation.

It is well documented that cholesterol aids in the formation of PI $(4,5)P_2$ domains in the absence and presence of Ca^{2+} (Ilya et al., 2009;

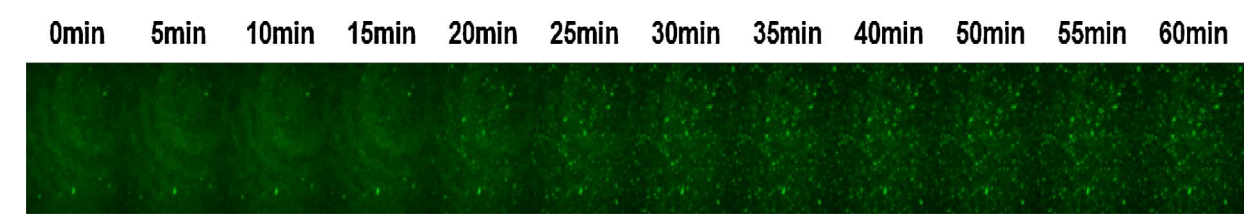


Fig. 7. TIRF images for a single position showing domain formation due to the interaction of Ca^{2+} with a homogenous SLB composed of 5%PI(4,5)P₂/0.1\%TopFlourPI(4,5)P₂/94.9\% DOPC. The membrane was imaged once every 5 min for an hour with a continuous flow of Ca^{2+} over the SLB. The high fluorescence regions appear after about 15–20 min. These high-intensity regions are thought to be due to the clustering of PI(4,5)P₂ and it fluorophores due to Ca^{2+} interaction (for better image quality, please see the movie in the Supplementary material).

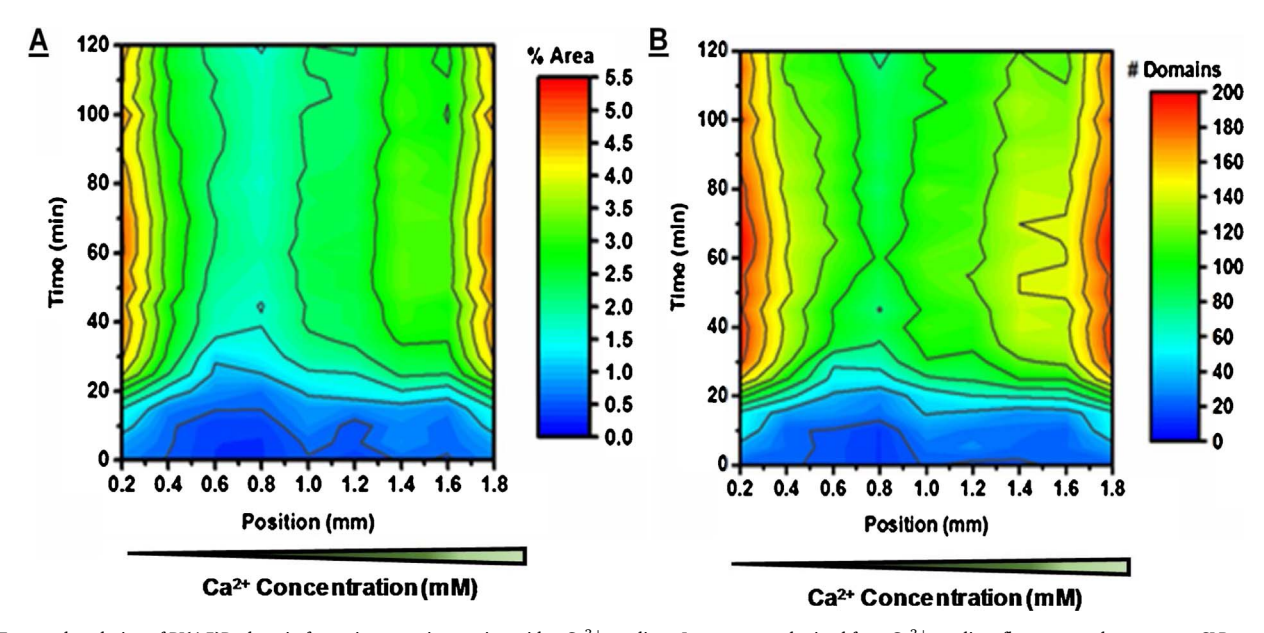


Fig. 8. Temporal evolution of $PI(4,5)P_2$ domain formation upon interaction with a Ca^{2+} gradient. Images were obtained for a Ca^{2+} gradient flown over a homogenous SLB composed of $5\%PI(4,5)P_2/0.1\%TopFlourPI(4,5)P_2/94.9\%DOPC$. The original data set was acquired by rastering the objective across the 2 mm observation chamber perpendicular to fluid flow, taking a total of nine images once every 5 min for an hour. The raw images were analyzed in ImageJ software (A) Number of $PI(4,5)P_2\%$ Area vs. time and location across the observation chamber (B) Domain number vs. time and location. To define a "domain", for each image a threshold was set that distinguished the high-intensity areas from the background and then converted to a binary image. From this, each measurement compiled and the topology graphs constructed. Domains first appear at approximately 15 min after flow begins. By the end of the experiment, the domain number spans from about 100 to 400 domains. The number of domains as well as the area occupied by the domains is largest for the area with the highest Ca^{2+} concentration.

Taglieri et al., 2012; Wang et al., 2016). We would, therefore, expect that for the same experimental conditions as described above, the presence of cholesterol will cause domains to form faster and to grow to larger sizes. Fig. 9 shows the development of PI(4,5)P2/cholesterol domains upon interaction with Ca2+ for one image area as a function of time, while the data in Fig. 10 illustrate the development of the PI(4,5) P₂/cholesterol domains upon interaction with a Ca²⁺ gradient. The Ca²⁺ has less impact on the cholesterol/PI(4,5)P₂/DOPC SLB morphology (Fig. 9) than that observed in the absence of cholesterol (Fig. 7). For the cholesterol-containing SLB, PI(4,5)P₂ enriched domains can be seen even in the absence of Ca^{2+} (prior to the addition of Ca^{2+}). In particular, for the regions with lower Ca²⁺ concentrations (1 mM and 2 mM Ca2+), where for the cholesterol free SLB only moderate domain formation occurred, an increased number of domains are found. From a kinetic point of view, the plateau where no additional domain formation is observed is reached faster (about 25 min after the Ca²⁺ was introduced in the chamber, see Fig. 10). Furthermore, there is less domain size disparity; without the cholesterol, the domain sizes ranged from 5 to 15 pixels, while in the presence of cholesterol the size range is 10-13 pixels. This is likely due to the domain stabilizing effects of cholesterol, which leads to larger domain size. The percent domain area plot shows for the SLB with cholesterol a shallower gradient as compared with PI(4,5)P2 only. These results are in agreement with the earlier formulated hypothesis that cholesterol stabilizes PI(4,5)P2 domains, i.e., while an additional PI(4,5)P2 domain forming effect is observed in the presence of Ca^{2+} , the impact of the Ca^{2+} on domain formation is less profound than in the absence of cholesterol (Ilya et al., 2009; Taglieri et al., 2012). The edge effects are also less pronounced in this experiment as compared to the former.

These three experiments, $PI(4,5)P_2$, $PI(4,5)P_2$ /Cholesterol, and POPS (in a DOPC SLB) show domain formation as an effect of Ca^{2+} exposure. As expected, the extent of domain formation is highly dependent on the Ca^{2+} concentration as evidenced by the Ca^{2+} gradient dependent kinetics of anionic lipid domain formation. These experiments underscore the versatility of the microfluidic device because not only can we successfully produce lipid bilayers exhibiting a lipid gradient but it is also possible to expose a homogenous bilayer to a gradient of a solute in the aqueous phase, which triggers a gradient specific response.

In addition to what has so far been discussed, we have discovered an unexpected but highly welcomed side effect of using the microfluidic device. SLBs that contain highly negatively charged lipids are usually challenging to form. We have found with our method that the microfluidic device helps with the SLB formation (fewer defects in comparison to more traditional methods (Jonsson et al., 2009)). We attribute this to the shear forces the vesicles experience as they are entering the observation chamber, which apparently leads to a better settling of the lipid bilayer onto the glass support. While we have not tested this exhaustively, we expect that the use of the microfluidic device will expand the scope with respect to lipid composition, allowing us to

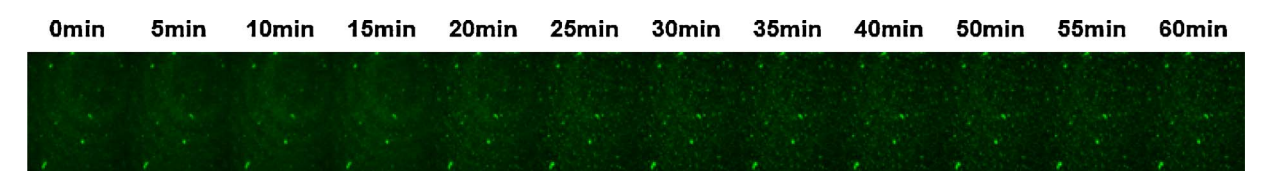


Fig. 9. TIRF images for a single area showing domain formation due to the interaction of Ca^{2+} with a homogenous SLB composed of $5\%PI(4,5)P_2/0.1\%TopFlourPI(4,5)P_2/30\%Cholesterol/64.9\%DOPC. The SLB was imaged once every 5 min for an hour with a continuous flow of the <math>Ca^{2+}$ gradient over the SLB. The high fluorescence regions appear after a period of 15 min of Ca^{2+} flow. These high-intensity regions are thought to be due to the clustering of $PI(4,5)P_2/TopFlourPI(4,5)P_2$ due to the interaction with Ca^{2+} . In comparison to the bilayer without cholesterol, there are more large domains at the start of the experiment. This is line with the hypothesis that cholesterol stabilizes these fluid $PI(4,5)P_2$ domains. (for better image quality, please see the movie in the Supplementary material).

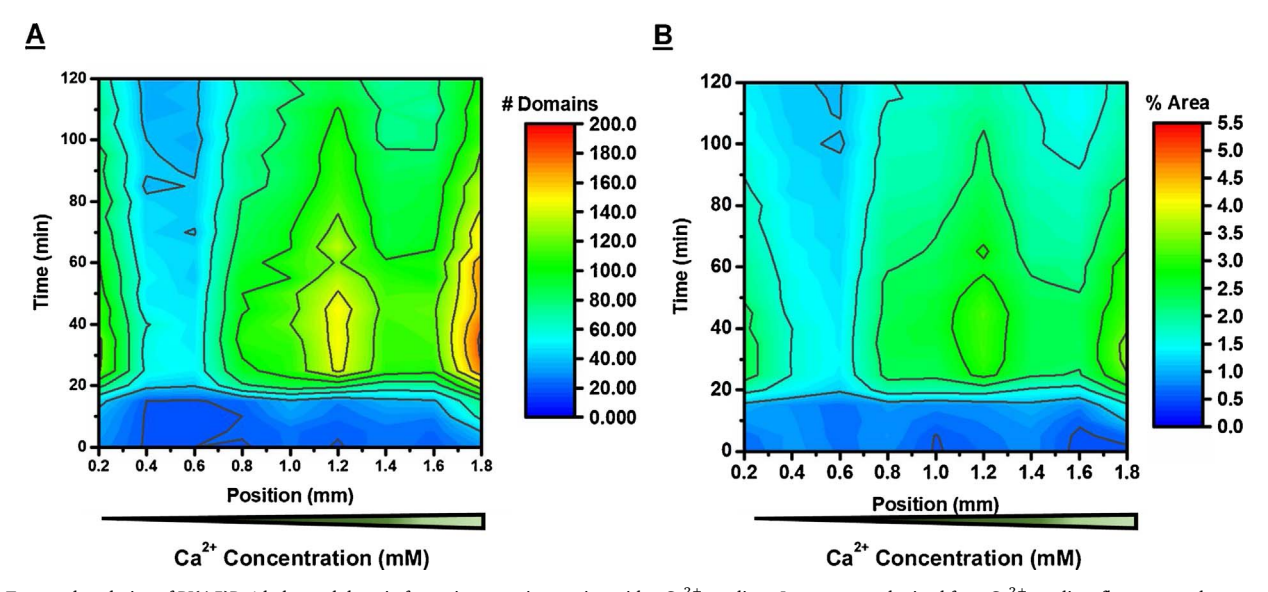


Fig. 10. Temporal evolution of $PI(4,5)P_2/c$ holesterol domain formation upon interaction with a Ca^{2+} gradient. Images were obtained for a Ca^{2+} gradient flown over a homogenous SLB composed of $5\%PI(4,5)P_2/0.1\%$ TopFlourPI(4,5) $P_2/30\%$ Cholesterol/64.9%DOPC. The original data set was acquired by rastering the objective across the 2 mm observation chamber perpendicular to fluid flow, taking a total of nine images once every 5 min for an hour. The raw images were analyzed in ImageJ software (A) Number of $PI(4,5)P_2/c$ holesterol domains vs. time and location across the observation chamber. (B) Percent domain area relative to the total field of view vs. time and location. To define a "domain", for each image a threshold was set that distinguished the high-intensity areas from the background and then converted to a binary image. From this, each measurement compiled and the topology graphs constructed. Domains first appear at approximately 15 min after flow begins. By the end of the experiment, the domain number spans from about 100 to 400 domains. The number of domains as well as the area occupied by the domains is largest for the area with the highest Ca^{2+} concentration.

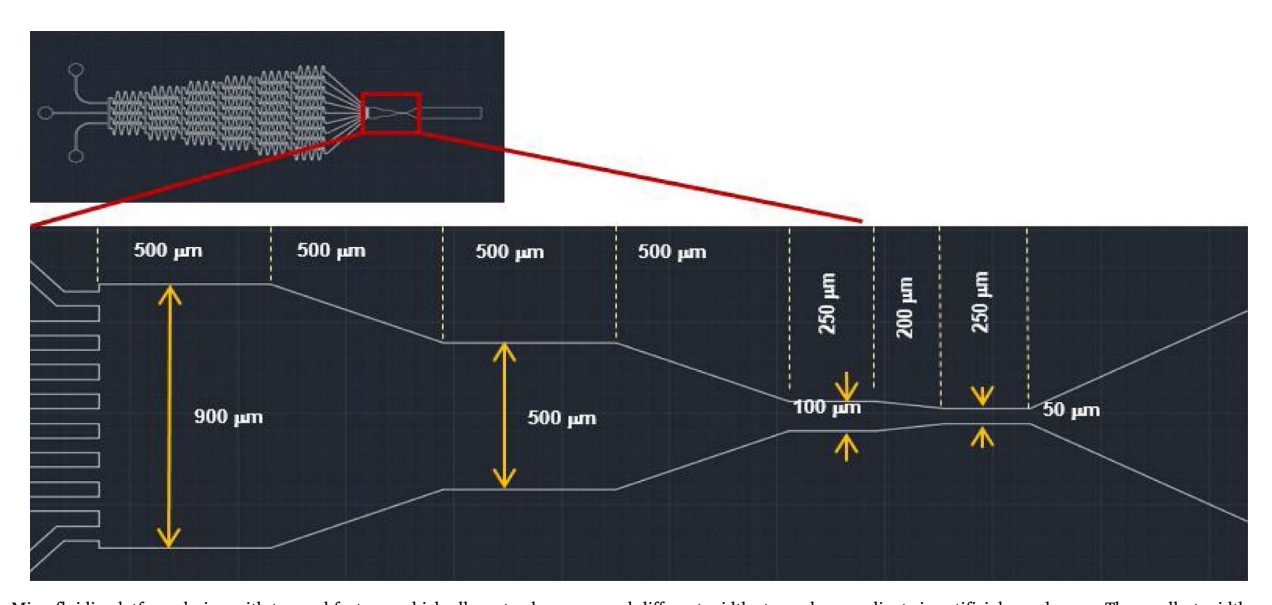


Fig. 11. Microfluidic platform design with tapered features which allows to choose several different widths to explore gradients in artificial membranes. The smallest widths are at the maximal end of large cell diameters allowing us to conduct more physiologically relevant experiments.

conduct experiments with more complicated, physiologically relevant lipid compositions.

Despite the robustness of the experiments described above, we realize that the size of the observation channel is too large to accomplish one of our goals, which is to investigate lipid gradients at physiologically relevant length scales. The comparatively large size of the observation channel presents a two-fold problem. (1) From a logistical point of view, the experiments take far too long, over 24 h, for the gradient to come to equilibrium. This not only limits throughput, but it also requires control of all experimental parameters (e.g., temperature) over quite long time periods. (2) Physiologically relevant length scales are in the range of tens of microns, while our observation chamber has a width of 2 mm. With this in mind, we fabricated a different microfluidic platform with a design based on a device developed by the Whitesides group (Jeon et al., 2000).

4.4. Microfluidic gradient generator with physiologically relevant length scales

Fig. 11 shows the dimensions of the microfluidic device with a tapered design. There are several choices of observation widths ranging from 900 μm down to 50 μm . The large size would be used for experiments where one wants to look at several frames of similar membrane composition, providing replicates of an experiment from a single microfluidic setup. The 100- μm and 50- μm size chambers are useful for studying effects in the SLB at length scales that are similar to large cells. Also at 100 μm , the entire channel can fit in the field of view of the microscope, making it unnecessary to stitch images together to acquire gradient information (Fig. 12).

To test whether the gradient in the fluid phase is maintained throughout the entire device, we conducted an experiment with a

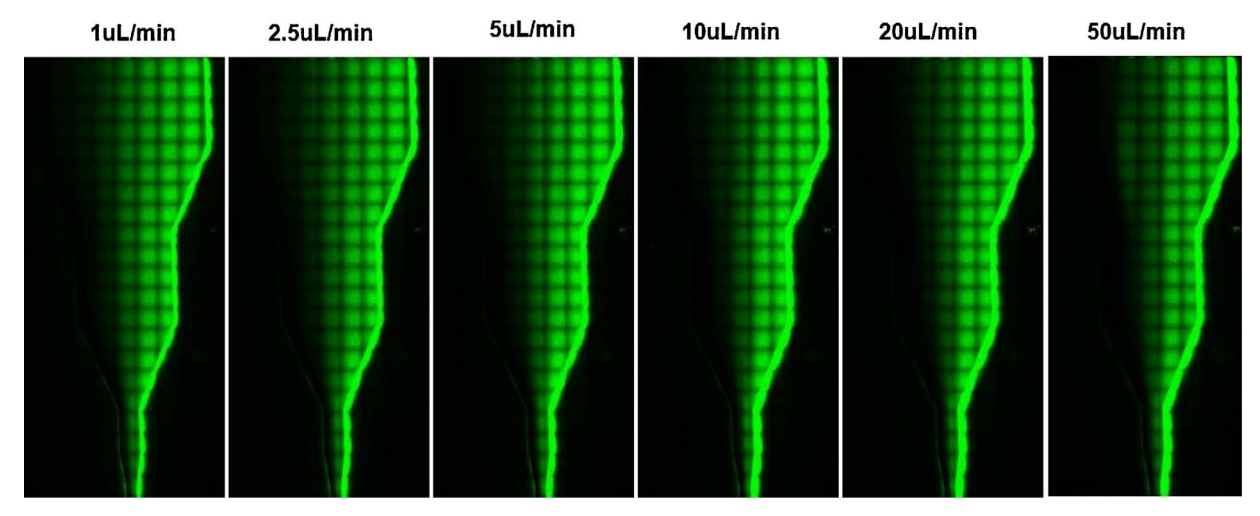
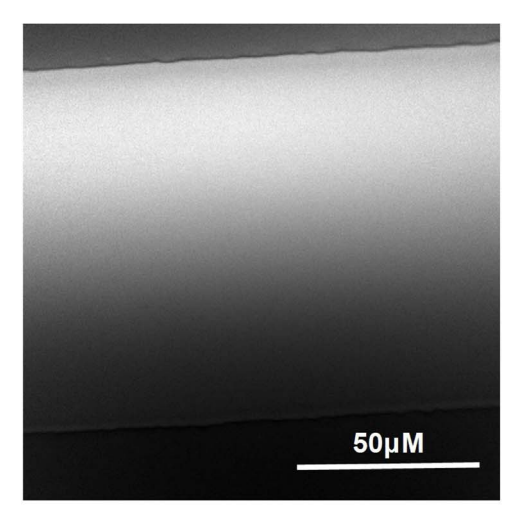


Fig. 12. TIRF images of a fluorescein gradient flowing through the tapered microfluidic device at different flow rates. Despite the tapered design, the gradient in the aqueous phase is maintained. These experiments highlight the effect of the flow rate on the steepness of the gradient. For the slowest flow rate the gradient is smooth and integrated, while for high flow rates the fluorescence intensity has the form of a step function.



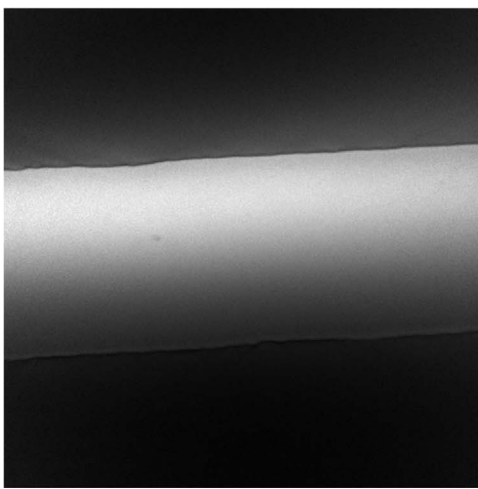


Fig. 13. Image of the fluorescein gradient in the two narrowest chambers. The gradient is well maintained throughout the entire microfluidic device.

fluorescein (Fig. 12 a pure glass substrate with no SLB). The experiment was carried out at several different flow rates to illustrate how the steepness and functional form of the gradient can be manipulated. For the highest flow rates, the gradient assumes the form of a step function, while at slower flow rates the gradient is smooth. Most importantly,

there is a gradient of fluorescein throughout the entire tapered design, even in the last compartment with the smallest dimension (Fig. 13). As the last step, we tested the tapered design by performing the TopFluor $^{\circ}$ PI(4,5)P $_2$ SLB insertion experiment in the same way as described above for the conventional microfluidic device. Fig. 14 shows two images from the beginning and end of a movie showing TopFluor $^{\circ}$ PI(4,5)P $_2$ inserting as a gradient (see Supplementary material for the movie). The gradient comes to equilibrium corresponding to the size of the channel, *i.e.* the smallest channel equilibrates quickest (\sim 10 min), while for the largest channel it takes the longest (\sim 10 h). With this design, we now have access to PI(4,5)P $_2$ gradients on membranes with physiological dimensions and realistically testable time spans (Figs. 14 and 15).

5. Conclusion

Cells have micron scale control over their plasma membrane morphology as seen by the formation of lipid and protein gradients during processes like chemotaxis or cytokinesis. We have developed a device that enables the fabrication of solid supported lipid bilayers that exhibit a lateral gradient with respect to their lipid composition. In addition, we have shown that we can elicit a gradient specific response in a homogenous lipid bilayer when this bilayer is in contact with a fluid that exhibits a gradient of one or more of its components.

We have successfully generated a $PI(4,5)P_2$ gradient which is testable and robust. We can make the SLB *in situ* on the TIRF microscope by either floating a gradient of monomeric lipid molecules over the preformed SLB or by laying down vesicles that exhibit differences in lipid composition. Ca^{2+} gradient-dependent domain formation on PI $(4,5)P_2$, PI $(4,5)P_2$ /Cholestrol, and PS-containing membranes illustrates that we can elicit a gradient specific response when a homogeneous SLB is exposed to an appropriate gradient in the fluid phase. This opens up the opportunity to use a gradient of protein, *e.g.*, a lipid modifying enzyme, in the fluid phase and to study the spatiotemporal response in the lipid bilayer. With the most recent iteration of our platform, we can generate a gradient on length scales typical for large cells.

In the future, we plan to use this platform to quantitatively ascertain the stochastic balance between the phosphatase PTEN and the kinase PI3K as these proteins interact with a PI(4,5)P $_2$ containing bilayer. We hope to fill gaps in the current mechanistic understanding of motility and cancer metastasis work. Such dynamic protein competition on laterally non-homogeneous SLBs, as we have developed in this study, would be a highly interesting target to investigate.

Fig. 14. Shows the first TIRF stitch image of TopFlourPI(4,5)P $_2$ inserted as a gradient in SLB composed of DOPC and the final image after the PI (4,5)P $_2$ gradient comes to equilibrium.

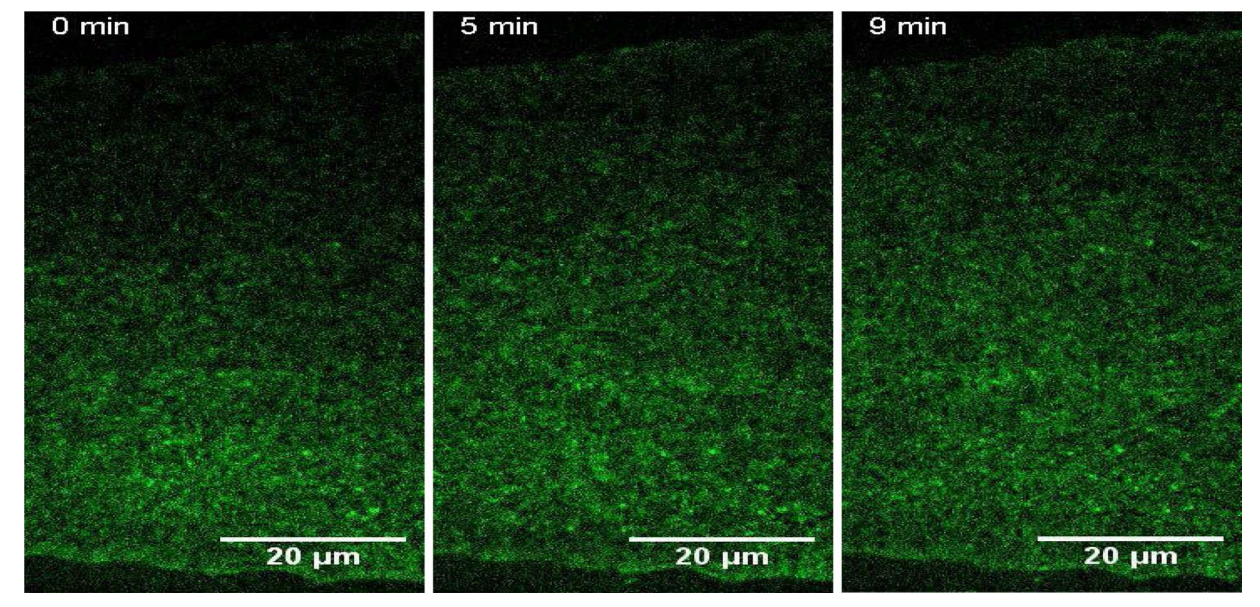


Fig. 15. Is the zoomed in area montage of the TopFlourPI(4,5)P2 experiments showing the gradient in the narrow chambers.

Conflicts of interest

None.

Funding

Dr. Gericke reports grants from National Science Foundation (CHE 1508499), during the conduct of this study.

Acknowledgement

This work was supported by a grant from the NSF Chemistry Division CHE 1508499.

Appendix A. Supplementary data

Supplementary data associated with this article can be found, in the online version, at https://doi.org/10.1016/j.chemphyslip.2017.10.007.

References

- Braunger, J.A., Kramer, C., Morick, D., Steinem, C., 2013. Solid supported membranes doped with PIP: influence of ionic strength and pH on bilayer formation and membrane organization. Langmuir 29, 14204–14213.
- Byfield, F.J., Wen, Q., Levental, I., Nordstrom, K., Arratia, P.E., Miller, R.T., Janmey, P.A., 2009. Absence of filamin A prevents cells from responding to stiffness gradients on gels coated with collagen but not fibronectin. Biophys. J. 96, 5095–5102.
- Castellana, E.T., Cremer, P.S., 2006. Solid supported lipid bilayers: from biophysical studies to sensor design. Surf. Sci. Rep. 61, 429–444.
- Cauvin, C., Echard, A., 2015. Phosphoinositides: lipids with informative heads and mastermind functions in cell division. Biochim. Biophys. Acta (BBA) - Mol. Cell Biol. Lipids 1851, 832–843.
- De Craene, J.O., Bertazzi, D.L., Bar, S., Friant, S., 2017. Phosphoinositides, major actors in membrane trafficking and lipid signaling pathways. Int. J. Mol. Sci. 18.
- Dertinger, S.K.W., Chiu, D.T., Jeon, N.L., Whitesides, G.M., 2001. Generation of gradients having complex shapes using microfluidic networks. Anal. Chem. 73, 1240–1246.
- Devreotes, P., Horwitz, A.R., 2015. Signaling networks that regulate cell migration. Cold Spring Harb. Perspect. Biol. 7.
- Drucker, P., Grill, D., Gerke, V., Galla, H.J., 2014. Formation and characterization of supported lipid bilayers containing phosphatidylinositol-4,5-bisphosphate and cholesterol as functional surfaces. Langmuir 30, 14877–14886.
- Dyson, J.M., Fedele, C.G., Davies, E.M., Becanovic, J., Mitchell, C.A., 2012. Phosphoinositide phosphatases: just as important as the kinases. Sub-cell. Biochem. 58, 215–279.
- Echard, A., 2008. Membrane traffic and polarization of lipid domains during cytokinesis. Biochem. Soc. Trans. 36, 395–399.
- Ellingson, J.S.L., William, E.M., 1968. Phospholipid reactivation of plasmalogen metabolism. Lipids 3, 111–120.
- Feigenson, G.W., 1986. On the nature of calcium ion binding between phosphatidylserine lamellae. Biochemistry 25, 5819–5825.
- Feigenson, G.W., 1989. Calcium-ion binding between lipid bilayers-the 4-component system of phosphatidylserine, phosphatidylcholine, calcium chloride, and water. Biochemistry 28, 1270–1278.
- Florine, K.I., Feigenson, G.W., 1987. Influence of the calcium-induced gel phase on the behavior of small molecules in phosphatidylserine and phosphatidylserine phosphatidylcholine mulilamellar vesicles. Biochemistry 26, 1757–1768.
- Gassama-Diagne, A., Payrastre, B., 2009. Phosphionositide signaling pathways: promising role as builders of epithelial cell polarity. In: In: Jeon, K.W. (Ed.), International Review of Cell and Molecular Biology, vol. 273, pp. 313–343.
- Review of Cell and Molecular Biology, vol. 273. pp. 313–343.

 Hardy, G.J., Nayak, R., Zauscher, S., 2013. Model cell membranes: techniques to form complex biomimetic supported lipid bilayers via vesicle fusion. Curr. Opin. Colloid Interface Sci. 18, 448–458.
- Harishchandra, R.K., Neumann, B.M., Gericke, A., Ross, A.H., 2015. Biophysical methods for the characterization of PTEN/lipid bilayer interactions. Methods 77–78, 125–135.
 Hauser, H., Chapman, D., Dawson, R.M., 1969. Physical studies of phospholipids. XI.
- Ca2+ binding to monolayers of phosphatidyserine and phosphatidylinositol.
 Biochim. Biophys. Acta 183, 320–333.
- Ilya, L., Christian, D.A., Wang, Y.-H., Madara, J.J., Discher, D.E., Janmey, P.A., 2009. Calcium-dependent lateral organization in phosphatidylinositol (4,5) bisphosphate (PIP2)- and cholesterol-containing monolayers. Biochemistry 48, 8241–8248.
- Jönsson, P., Beech, J.P., Tegenfeldt, J.O., Höök, F., 2009. Shear-driven motion of supported linid bilayers in microfluidic channels. J. Am. Chem. Soc. 131, 5294–5297.
- Jeon, N.L., Dertinger, S.K.W., Chiu, D.T., Choi, I.S., Stroock, A.D., Whitesides, G.M., 2000. Generation of solution and surface gradients using microfluidic systems. Langmuir 16, 8311–8316.
- Jonsson, P., Beech, J.P., Tegenfeldt, J.O., Hook, F., 2009. Shear-driven motion of supported lipid bilayers in microfluidic channels. J. Am. Chem. Soc. 131, 5294–5297.
- Kalb, E., Frey, S., Tamm, L.K., 1992. Formation of supported planar bilayers by fusion of vesicles to supported phospholipid monolayers. Biochim. Biophys. Acta 1103, 307–316
- Keller, C.A., Glasmastar, K., Zhdanov, V.P., Kasemo, B., 2000. Formation of supported membranes from vesicles. Phys. Rev. Lett. 84, 5443–5446.
- Knight, J.D., Falke, J.J., 2009. Single-molecule fluorescence studies of a PH domain: new insights into the membrane docking reaction. Biophys. J. 96, 566–582.
- Knight, J.D., Lerner, M.G., Marcano-Velazquez, J.G., Pastor, R.W., Falke, J.J., 2010. Single molecule diffusion of membrane-bound proteins: window into lipid contacts and bilayer dynamics. Biophys. J. 99, 2879–2887.
- Krabbenborg, S.O., van Weerd, J., Karperien, M., Jonkheijm, P., Huskens, J., 2014.

- Locked-in biomimetic surface gradients that are tunable in size, density and functionalization. ChemPhysChem 15, 3460–3465.
- Krahn, M.P., Wodarz, A., 2012. Phosphoinositide lipids and cell polarity: linking the plasma membrane to the cytocortex. Essays Biochem. 53, 15–27.
- Liu, K.N., Hung, C.M.S., Swift, M.A., Munoz, K.A., Cortez, J.L., Sanii, B., 2015. Configurable lipid membrane gradients quantify diffusion, phase separations and binding densities. Soft Matter 11, 8217–8220.
- Luna, C., Stroka, K.M., Bermudez, H., Aranda-Espinoza, H., 2011. Thermodynamics of monolayers formed by mixtures of phosphatidylcholine/phosphatidylserine. Colloids Surf. B-Biointerfaces 85, 293–300.
- Mangold, H.K., Malins, D.C., 1960. J. Am. Oil Chem. Soc. 11, 576-587.
- Mangold, H.K., 1961. J. Am. Oil Chem. Soc. 38, 708-727.
- Marsh, D., 2013. Handbook of Lipid Bilayers, 2nd edition. .
- Moens, P.D., Bagatolli, L.A., 2007. Profilin binding to sub-micellar concentrations of phosphatidylinositol(4,5)bisphosphate and phosphatidylinositol (3,4,5) trisphosphate. Biochim. Biophys. Acta 1768, 439–449.
- Richter, R.P., Bérat, R., Brisson, A.R., 2006. Formation of solid-supported lipid bilayers: an integrated view. Langmuir 22, 3497–3505.
- Roux, M., Bloom, M., 1991. Calcium-binding by phosphatidylserine headgroups-deuterium NMR study. Biophys. J. 60, 38–44.
- Saarikangas, J., Zhao, H., Lappalainen, P., 2010. Regulation of the actin cytoskeletonplasma membrane interplay by phosphoinositides. Physiol. Rev. 90, 259–289.
- Sackmann, E.K., Fulton, A.L., Beebe, D.J., 2014. The present and future role of microfluidics in biomedical research. Nature 507, 181–189.
- Sasaki, T., Takasuga, S., Sasaki, J., Kofuji, S., Eguchi, S., Yamazaki, M., Suzuki, A., 2009. Mammalian phosphoinositide kinases and phosphatases. Prog. Lipid Res. 48, 207, 242
- Sbalzarini, I.F., Koumoutsakos, P., 2005. Feature point tracking and trajectory analysis for video imaging in cell biology. J. Struct. Biol. 151, 182–195.
- Schindelin, J., Rueden, C.T., Hiner, M.C., Eliceiri, K.W., 2015. The ImageJ ecosystem: an open platform for biomedical image analysis. Mol. Reprod. Dev. 82, 518–529.
- Schutz, G.J., Schindler, H., Schmidt, T., 1997. Single-molecule microscopy on model membranes reveals anomalous diffusion. Biophys. J. 73, 1073–1080.
- Shekhar, P., Nanda, H., Losche, M., Heinrich, F., 2011. Continuous distribution model for the investigation of complex molecular architectures near interfaces with scattering techniques. J. Appl. Phys. 110, 12.
- Sims, R.P.A., Larose, J.A.G., 1962. The use of iodine vapor as a general detecting agent in the thin layer chromatography of lipids. J. Am. Oil Chem Soc. 39, 232.
- Sinn, C.G., Antonietti, M., Dimova, R., 2006. Binding of calcium to phosphatidylcholinephosphatidylserine membranes. Colloid Surf. A-Physicochem. Eng. Asp. 282, 410–419.
- Skipski, V.P., Peterson, R.F., Barclay, M., 1962. J. Lipid Res. 3.
- Slochower, D.R., Wang, Y.H., Tourdot, R.W., Radhakrishnan, R., Janmey, P.A., 2014. Counterion-mediated pattern formation in membranes containing anionic lipids. Adv. Colloid Interface Sci. 208, 177–188.
- Subbarow, F., 1925. J. Biol. Chem. 374-389.
- Taglieri, D.M., Delfin, D.A., Monasky, M.M., 2012. Cholesterol regulation of PIP(2): why cell type is so important. Front. Physiol. 3, 492.
- Toh, A.G.G., Wang, Z.P., Yang, C., Nguyen, N.T., 2014. Engineering microfluidic concentration gradient generators for biological applications. Microfluid. Nanofluid. 16, 1–18
- Tsujita, K., Itoh, T., 2015. Phosphoinositides in the regulation of actin cortex and cell migration. Biochim. Biophys. Acta 1851, 824–831.
- Vernier, P.T., Ziegler, M.J., Dimova, R., 2009. Calcium binding and head group dipole angle in phosphatidylserine-phosphatidylcholine bilayers. Langmuir 25, 1020–1027.
- Viaud, J., Mansour, R., Antkowiak, A., Mujalli, A., Valet, C., Chicanne, G., Xuereb, J.-M., Terrisse, A.-D., Séverin, S., Gratacap, M.-P., Gaits-Iacovoni, F., Payrastre, B., 2016. Phosphoinositides: important lipids in the coordination of cell dynamics. Biochimie 125, 250–258.
- Wang, Y.H., Slochower, D.R., Janmey, P.A., 2014. Counterion-mediated cluster formation by polyphosphoinositides. Chem. Phys. Lipids 182, 38–51.
- Wang, Y.H., Bucki, R., Janmey, P.A., 2016. Cholesterol-dependent phase-demixing in lipid bilayers as a switch for the activity of the phosphoinositide-dinding cytoskeletal protein gelsolin. Biochemistry 55, 3361–3369.
- Ziemba, B.P., Falke, J.J., 2013. Lateral diffusion of peripheral membrane proteins on supported lipid bilayers is controlled by the additive frictional drags of (1) bound lipids and (2) protein domains penetrating into the bilayer hydrocarbon core. Chem. Phys. Lipids 172, 67–77.